Journal of Catalysis 278 (2011) 288–296

Contents lists available at ScienceDirect

Journal of Catalysis

journal homepage: www.elsevier.com/locate/jcat

Structural changes of Au–Cu bimetallic catalysts in CO oxidation: In situ XRD, EPR, XANES, and FT-IR characterizations

Xiaoyan Liu [a,b], Aiqin Wang [a], Lin Li [a], Tao Zhang [a,*], Chung-Yuan Mou [b,*], Jyh-Fu Lee [c]

[a] Dalian Institute of Chemical Physics, Chinese Academy of Sciences, Dalian 116023, China
[b] Department of Chemistry, National Taiwan University, Taipei 10617, Taiwan
[c] National Synchrotron Radiation Research Center, Hsinchu 30076, Taiwan

ARTICLE INFO

Article history:
Received 22 November 2010
Revised 23 December 2010
Accepted 23 December 2010
Available online 28 January 2011

Keywords:
Gold
Copper
Bimetallic
CO oxidation
XANES
EPR
FT-IR
In situ XRD

ABSTRACT

Au–Cu bimetallic nanoparticles supported on SBA-15 have been reported to be much more active in CO oxidation than the corresponding monometallic counterparts in our previous work. In this work, in situ techniques including XRD, EPR, XANES, and FT-IR were employed to reveal the structural changes of the Au–Cu bimetallic particles during different pretreatment and reaction conditions, and to clarify the essence of the synergistic effect between gold and copper. The results showed that gold remained as Au^0 in any treatment conditions, while copper was very sensitive to the treatment temperature and atmosphere. The freshly reduced catalyst was a mixture of Au_3Cu_1 intermetallic phase and Cu_2O amorphous phase. In CO oxidation, the Au_3Cu_1 intermetallic phase was segregated into a gold core decorated with tiny CuO_x patches, and CO adsorbed on Au^0 reacted with active oxygen provided by the neighboring CuO_x, thus enhancing greatly the activity for CO oxidation.

1. Introduction

Bimetallic nanoparticles frequently exhibit better catalytic performances than their monometallic counterparts and have therefore attracted a great deal of attention from both academic and industrial fields. For example, Au–Pd bimetallic nanoparticles are efficient catalysts for a number of selective oxidation reactions [1–4], Pt–Ru bimetallic catalyst is a well-known catalyst for fuel cells [5–7], and Pd–Ag bimetallic systems are widely used as selective hydrogenation catalysts [8–10]. Generally, the synergy between the two components of a bimetallic catalyst can be understood in terms of assemble and ligand effects, i.e., one component may serve as a spacer to isolate the active sites [11,12] or as an electronic modifier to the other component [2,13]. Experimentally, the catalytic performances of bimetallic nanoparticles are often influenced by a spectrum of factors, such as nanostructure, surface composition, particle size, and shape. The most featured aspects that distinguish a bimetallic catalyst from monometallic ones are the tunable nanostructures and surface compositions. A bimetallic nanostructure can be a random alloy, a core–shell structure, or just mixed monometallic nanoparticles. These different nanostructures give rise to different catalytic performances, as shown by the excellent work of Alayoglu et al. in which Ru@Pt core–shell architecture performed significantly better than the PtRu nano-alloys and mixtures of monometallic nanoparticles in PROX reaction [14]. Closely related with the nanostructure, the surface composition is another important factor affecting the catalytic behavior. It is known that the surface composition of a bimetallic catalyst can be markedly different from that of the bulk when surface segregation occurs. Surface segregation is a common phenomenon for the bimetallic catalysts, and it is not only influenced by the intrinsic properties of the two components such as bond strengths and surface energies but also determined by the external conditions such as temperatures and atmospheres during the pretreatment and reaction processes [15]. For a given bimetallic system, although the surface segregation propensity can be predicted to some extent based on density functional calculations [16], it may be very different from the real case where both temperature and atmosphere can induce segregation of the bimetallic catalyst. Therefore, it is very important to investigate the possible changes of nanostructure and surface composition under the real reaction conditions so that the governing factors responsible for the catalytic activity can be elucidated.

* Corresponding authors. Address: Dalian Institute of Chemical Physics, Chinese Academy of Sciences, 457 Zhongshan Road, Dalian 116023, China. Fax: +86 411 84691570 (T. Zhang), +886 2 23660954 (C.-Y. Mou).
E-mail addresses: taozhang@dicp.ac.cn (T. Zhang), cymou@ntu.edu.tw (C.-Y. Mou).

0021-9517/$ - see front matter © 2010 Elsevier Inc. All rights reserved.
doi:10.1016/j.jcat.2010.12.016

Gold-based bimetallic nanoparticles are emerging as a type of efficient catalysts in a variety of important reactions including low-temperature CO oxidation [17–19], epoxidation of propene [20], hydrogenation of oxygen to produce hydrogen peroxide [21], selective oxidation of alcohols to aldehydes or ketones [22], and among others. In most of gold-containing bimetallic nanocatalysts, gold possesses a less oxophilicity than the other metals due to the larger electronegativity of gold, which may lead to a tendency of segregation of the alloy phase in oxidizing atmosphere with gold enriched in core while the other metal enriched on the surface [2,23]. Such changes, if occurred, will have a great influence on the activity and stability of gold-containing bimetallic catalysts during oxidation reactions. Therefore, it is interesting and important to study in situ the structural changes of the gold-based bimetallic nanoparticles during the reaction, in particular for oxidation reaction since it is one of the most important reactions catalyzed by gold.

We recently developed Au–Ag [24–29] and Au–Cu [30,31] bimetallic nanoparticles which showed a very high activity for low-temperature CO oxidation and a strong synergistic effect between Au and the second metal. Of particular importance is that when the second metal (Cu or Ag) was deposited on the gold particles [28–31], the resulting Au–Ag and Au–Cu bimetallic nanoparticles were rather stable against sintering induced by high-temperature calcinations. And this property makes the bimetallic nanoparticles much superior to monometallic gold and renders them great potentials in application in high-temperature environments such as for automobile emission control [32]. The anti-sintering behavior of the Au–Ag and Au–Cu bimetallic particles is interpreted as the segregation of the second metal (Ag or Cu) on the surface during high-temperature calcination, which results in the formation of silver or copper oxides on the surfaces of gold particles, thus protecting the gold particles from aggregation [28]. Such changes in the structure of the bimetallic nanoparticles trigger new questions: will the bimetallic structure be stable during the CO oxidation reaction? If not, what is the real active site (alloy or segregated structure)? What is the role of the second metal in the CO oxidation? To answer these questions, we took Au–Cu/SBA-15 bimetallic nanocatalyst as an example and employed a variety of in situ techniques including X-ray diffraction (XRD), electron paramagnetic resonance (EPR), diffuse reflectance infrared Fourier transform (DRIFT), and X-ray absorption near edge structure (XANES) to trace the structural changes during the CO oxidation reaction for identifying the genuine active sites.

2. Experimental

2.1. Preparation of catalysts

The Au–Cu/SBA-15 bimetallic nanocatalyst was prepared using a two-step method we reported previously [28–31]. In detail, prior to the metal deposition, SBA-15 support (home-made according to Zhao et al. [33]) was first functionalized with APTES ($H_2N(CH_2)_3$-$Si(OEt)_3$). Then, 20 mL of an aqueous tetrachloroaurate ($HAuCl_4$, 0.0115 M) solution was added to 1.0 g of APTES-SBA-15 followed by reduction with $NaBH_4$ (0.1 M). The change of the color from yellow to purple indicated gold particles were deposited onto the support. After thorough washing and filtration, the recovered solid was added to 20 mL of an aqueous solution of copper nitrate ($Cu(NO_3)_2{\cdot}3H_2O$, 0.0115 M) and again followed by reduction with $NaBH_4$. After thorough washing and filtration, the solid was dried at 110 °C, calcined at 500 °C in air for 6 h to obtain the Au–Cu/SBA-15 catalyst. The desired Au/Cu atomic ratio was 1/1, and the total metal loading was 6 wt.%. For comparison, the monometallic Au/SBA-15 and Cu/SBA-15 catalysts were also prepared by the similar method. The physical properties of the catalysts are shown in Table 1.

Table 1
Physical properties and chemical compositions of the catalysts.

Samples	Au/Cu (molar ratio)	Total metal loading (wt.%)	BET Surface area ($m^2\,g^{-1}$)	Average pore diameter (nm)
Au/SBA-15	1/0	5.99	568	6.7
Au–Cu/SBA-15	0.99/1	4.11	525	7.0
Cu/SBA-15	0/1	3.50	578	6.3

2.2. Catalytic test

The catalytic activity for CO oxidation was measured using a continuous flow fixed-bed reactor system. A feed gas containing 1.0 vol.% CO and 1.0 vol.% O_2 balanced with He was allowed to pass through the catalyst sample of 60 mg (20–40 mesh) at a flow rate of 20 mL min^{-1} (corresponding to a space velocity of 20,000 mL h^{-1} g_{cat}^{-1}). Prior to the reaction, the catalyst was pretreated with H_2 at 550 °C for 1 h, and then cooled to the reaction temperature under He. The inlet and outlet gas compositions were on-line analyzed by a gas chromatograph (HP 6890, TDX-01 column).

2.3. Characterizations

The actual metal loadings of the catalysts were determined by inductively coupled plasma spectrometer (ICP-AES) on an IRIS Intrepid II XSP instrument (Thermo Electron Corporation). Nitrogen adsorption–desorption measurements were performed at −196 °C with a Micromeritics ASAP2010 instrument. The average pore diameters were estimated with desorption branches based on BJH model, and the specific surface area was calculated by the BET equation.

In situ XRD patterns were collected on a PW3040/60 X' Pert PRO (PANalytical) diffractometer equipped with an in situ cell that allows heating and introduction of gases. The diffractometer was operated at 40 kV and 40 mA using Cu Kα radiation source (λ = 0.15432 nm). To trace the structural changes of the catalyst, 40 mg of a catalyst sample was loaded into the cell and heated up to 500 °C at a rate of 5 °C/min under a flow of 10 vol.% H_2/Ar (total flow: 20 mL min^{-1}), during which the XRD patterns were recorded using a continuous mode from 30° to 50° at a scanning speed of 5°/min. Then, the catalyst was cooled to RT under He, and followed by treatment under various reaction atmosphere. For CO oxidation atmosphere, a flow of 1 vol.% CO in air at a rate of 20 mL min^{-1} was used, while for PROX (preferential oxidation of CO in H_2) reaction atmosphere a gas flow containing 1 vol.% CO and 0.5 vol.% O_2 balanced with H_2 at a total flow rate of 40 mL min^{-1} was used. The reactions were run both in a temperature-increased mode and in an isothermal mode. The XRD patterns were recorded with time on stream or with temperature during the whole treatment.

EPR spectra were recorded at 150 K with a Bruker EMX spectrometer working in the X-band (9.53 GHz). A weighted catalyst sample of 20 mg was placed inside a 4-mm O.D. quartz tube with greaseless stopcocks which allows heating the sample at different atmosphere and evacuation without exposing to air. Before each EPR measurement, the sample that had been treated under various conditions was subsequently evacuated at room temperature until the residual pressure was below 1×10^{-3} Torr. The atmosphere used for treating the catalyst was respectively pure H_2 and CO oxidation gas composed of 4 vol.% CO and 4 vol.% O_2 balanced with He.

X-ray absorption near edge structure (XANES) spectra at Au L_{III}-edge and Cu K-edge were recorded at beamline 17C1 of National Synchrotron Radiation Research Center, Hsinchu, Taiwan. The electron storage ring is operated at 1.5 GeV and a beam current of 360 mA with a top-up injection mode. The beamline employs a double Si(1 1 1)-crystal monochromator for energy selection with a resolution $\Delta E/E$ better than 2×10^{-4}. The powdery catalysts were packed into the middle part of a quartz glass tube. Both ends of the tube are sealed with Kapton film. The reducing gas is pure H_2, and the reaction gas is composed of 1.6 vol.% CO and 1.6 vol.%O_2, balanced with He. All spectra were recorded at room temperature in a transmission mode. Cu foil or Au foil as standard compound was measured simultaneously by using the third ionization chamber so that energy calibration could be performed scan-by-scan. The X-ray absorption data were processed by Athena software package [34].

The DRIFT spectra were acquired with a spectrometer (Bruker Equinox 55) equipped with a MCT detector and operated at a resolution of 4 cm^{-1}. A concentration of 20 mg of a catalyst sample was loaded into the cell with a ZnSe window which allowed in situ treatment under various atmospheres from room temperature up to 500 °C. Before CO adsorption, the sample was in situ pre-reduced in pure H_2 at 500 °C for 1 h, and then cooled to 20 °C for collecting the background spectrum. Subsequently, the sample was exposed to a flowing mixture of 3.4 vol.% CO in He with a rate of 58 mL min^{-1} (denoted as CO atmosphere) or 3.3 vol.% CO, 3.3 vol.% O_2 and 93.4 vol.% He with a rate of 60 mL min^{-1} (denoted as CO oxidation atmosphere) at room temperature, and the spectrum was collected again. The spectra presented in the work were obtained by subtracting the corresponding background.

FT-IR spectra were measured at −110 °C with a Bruker Equinox 55 spectrometer in the absorbance mode with a resolution of 2 cm^{-1}. Self-supported wafers were prepared from the catalyst powder (ca. 20 mg). The sample wafers were loaded into a quartz IR cell with CaF_2 windows and in situ treated under pure H_2 flow at 500 °C for 1 h. After evacuation at the same temperature for 30 min, the samples were cooled to −110 °C, and 5 Torr of CO was admitted to the cell. After reaching the equilibrium, the cell was evacuated to remove gaseous CO. Subsequently, 2 Torr of pure O_2 was dosed into the cell and the spectra were recorded with time. By subtracting the spectrum of the background, the final IR spectra were obtained.

3. Results

3.1. Activity for CO oxidation

In our previous work [30], we have shown that Au–Cu/SBA-15 exhibited very high activities for both low-temperature CO oxidation and PROX reactions which were ascribed to a synergistic effect between Au and Cu. What is the essence of the synergy effect? Is it correlated with the structure or composition change of the bimetallic nanoparticles under different conditions? To clarify these questions, in the present work, we further investigated the effect of pretreatment conditions on the catalytic activity of the Au–Cu bimetallic nanoparticles supported on SBA-15. As shown in Fig. 1, the as-calcined Au–Cu/SBA-15 exhibited poor activity for CO oxidation; the light-off temperature was as high as 200 °C (curve a). However, after reduction treatment at 550 °C, the catalyst became very active; total conversion of CO was obtained at 25 °C (curve b). This is consistent with the pretreatment conditions of monometallic gold nanocatalysts reported in our previous work [35]. Following the first run from −50 to 350 °C in a temperature-increased mode, the catalyst was cooled to −50 °C under the reaction atmosphere and then subjected to the second run. It turned out that the catalyst gave a slightly higher activity in the second run (curve c). It means that the spent catalyst is even slightly more active than the freshly reduced catalyst. To further confirm this, the catalyst after the second run was again reduced at 550 °C for 2 h before starting the third run. As expected, the CO conversion curve (curve d) in the third run was almost the same as that in the first run. In these recycling tests, not any deactivation was observed. The TEM images of the sample before and after the reaction (not shown here) indicated that the sizes and the size distributions of the particles were not changed (remaining at ~3 nm) by the CO oxidation up to 400 °C, which can be one reason for the rather stable behavior of the catalyst in CO oxidation.

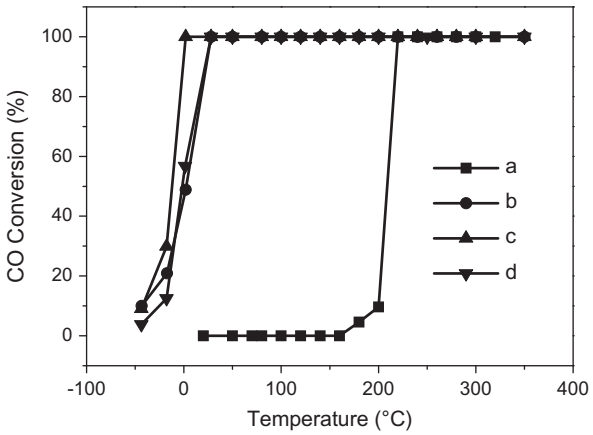

Fig. 1. CO conversions with the reaction temperature over Au–Cu/SBA-15 catalyst: (a) as-calcined sample; (b) freshly reduced sample; (c) the sample after the first run; (d) the sample after the second run was reduced again at 550 °C for 2 h under pure H_2.

3.2. In situ XRD

3.2.1. In situ XRD in H_2 atmosphere

The aforesaid reactivity test has shown that the Au–Cu catalyst became activated only after H_2 reduction at a high temperature. To trace the changes of the Au–Cu bimetallic nanostructure during the high-temperature reduction, we conducted in situ XRD examinations of the catalyst in H_2 atmosphere with elevating temperature. As shown in Fig. 2, the as-calcined sample presents a broad diffraction line at 38.2°, which can be indexed as gold (1 1 1) reflections [24–31]. No copper species were detected, suggesting that the copper species, most probably existing as CuO_x, are amorphous or their particle sizes are too small to be detected by XRD. However, with increasing the treatment temperature in H_2, the diffraction line shifts gradually to higher angle until a constant value of 39.2° was reached at above 325 °C, representing Au–Cu alloy formation process. Based on the Vegard's law ($a_{alloy} = xa_{Au} + (1-x)a_{Cu} + 0.01198x(1-x)$) [36], the molar fraction of gold (x) was calculated to be 0.77, which corresponds to an atomic ratio of gold to copper being about 3/1, suggesting that Au_3Cu_1 intermetallic alloy was formed [30,31,36]. However, the actual Au/Cu determined by ICP is 0.99/1 (Table 1). The discrepancy suggests that not all of the copper in the catalyst is alloyed with gold during the high-temperature reduction. The deficiency in Cu for the Au–Cu bimetallic structure was also reported by other group [37]. In addition, the diffraction line width remained essentially unchanged in the whole reduction process, indicating that the average particle size was not altered significantly by this high-temperature reduction treatment.

3.2.2. In situ XRD in CO oxidation atmosphere

After the aforementioned high-temperature reduction treatment, the Au–Cu nanoparticles became very active for CO

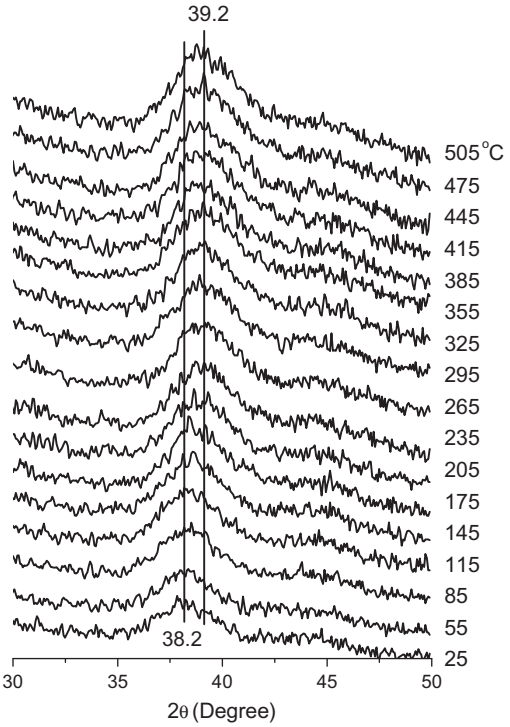

Fig. 2. In situ XRD patterns of the as-calcined Au–Cu/SBA-15 catalyst with increasing reduction temperature under H_2 atmosphere. The vertical lines indicate the 2θ position at 38.2° and 39.2°, respectively.

oxidation. Considering that the reaction gas for CO oxidation contains excess O_2 (CO/O_2 = 1/1 while the stoichiometric ratio is 1/0.5 in CO oxidation) and the copper in the alloy phase will have the tendency to segregate on the surface in such oxidizing atmosphere, in situ XRD was again employed to trace the structural changes under reaction conditions. As shown in Fig. 3a, during the CO oxidation at room temperature for more than 8 h, the diffraction line position slightly shifted toward lower angle, from 39.2° to 39.0°, while the diffraction line width remained unchanged. In contrast, when the reaction was carried out at elevated temperatures, evident diffraction line shift was observed toward lower angle until 38.2° at temperatures higher than 325 °C (Fig. 3b). As mentioned earlier, 38.2° represents a pure gold phase while 39.2° an Au_3Cu_1 alloy phase. Therefore, this result indicates that the gold–copper alloy phase was not stable during the course of CO oxidation, and the phase segregation became more pronounced with increasing the reaction temperature. When the reaction temperature was above 325 °C, nearly complete phase segregation took place as indicated by the disappearance of Au_3Cu_1 alloy phase and concurrent appearance of pure gold phase. More interesting, it was found that the structural change of the Au–Cu alloy nanoparticles was totally reversible. Upon being subjected to treatment with H_2 at elevated temperatures, the segregated structure again gradually changed into Au_3Cu_1 alloy phase, just like the case shown in Fig. 2.

3.2.3. In situ XRD in PROX atmosphere

When a large excess of H_2 was present in the reaction stream, the Au–Cu alloy catalyst still exhibited high activity and selectivity for the preferential oxidation of CO (PROX), as reported in the early work [30]. In such H_2-rich conditions, the Au–Cu alloy catalyst seems stable throughout the whole reaction process. As shown in Fig. 4, when the reaction proceeded either at a constant temperature (80 °C, Fig. 4a) or in a temperature-increased mode (Fig. 4b), the XRD patterns remained unchanged during the whole reaction

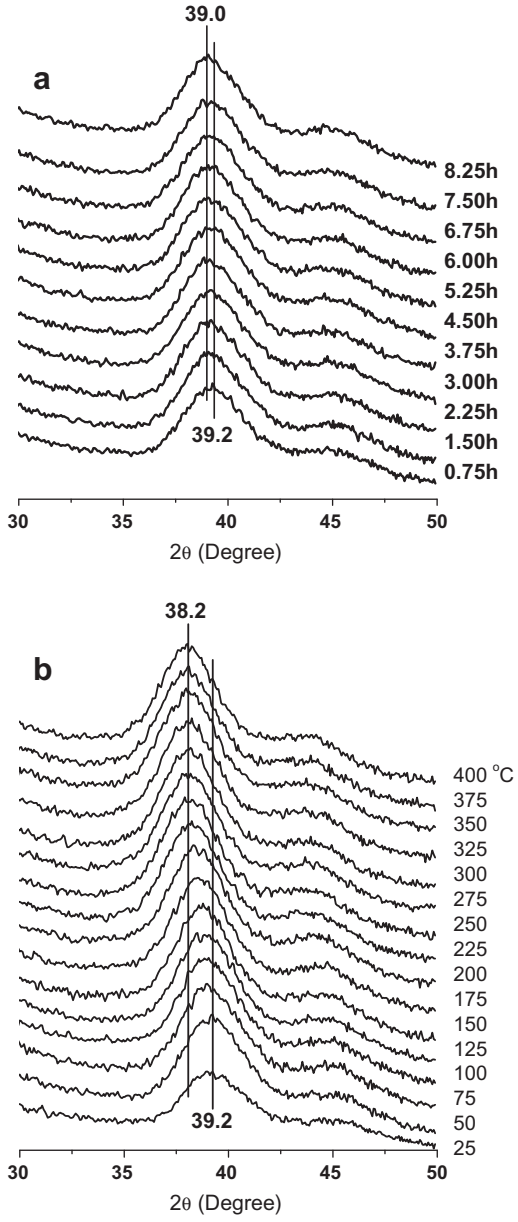

Fig. 3. In situ XRD patterns of the freshly reduced Au–Cu/SBA-15 catalyst with (a) time on stream at room temperature and (b) increasing temperature under CO oxidation atmosphere. The vertical lines indicate the 2θ positions at 38.2°, 39.0°, and 39.2°, respectively.

process, with the 2θ value of the diffraction line remaining at 39.2° which is characteristic of Au_3Cu_1 alloy phase. Clearly, such a reducing atmosphere is quite different from pure CO oxidation condition in affecting the Au–Cu nanostructure.

3.3. In situ EPR

Although in situ XRD examinations revealed the structural changes of Au–Cu nanoparticles in reducing or oxidizing atmosphere, the information about the Cu species is still lacking since they were not detectable by XRD. As conjectured earlier, the Cu component is highly probable to form CuO_x leading to a phase segregation of Au–Cu alloy during the CO oxidation process. The fact that the CuO_x species were not detectable may suggest that they are amorphous or their particle sizes are below the detection limit of XRD. To identify the CuO_x species, we employed in situ EPR

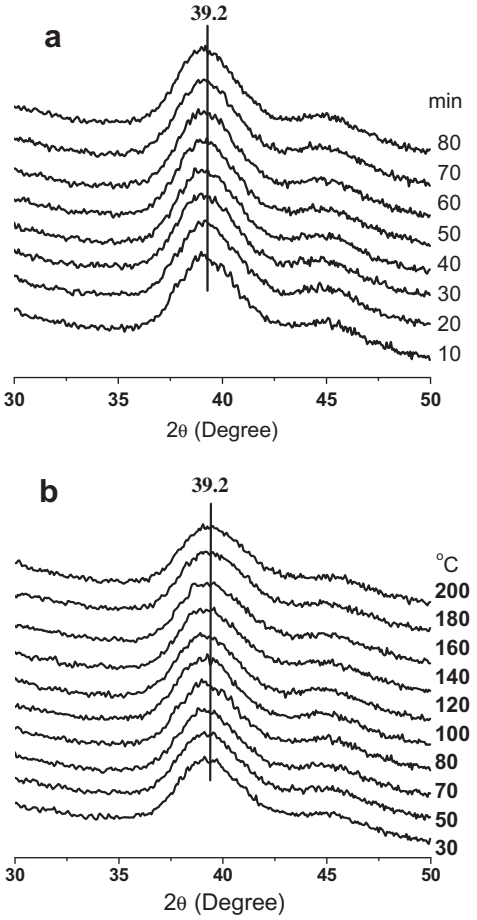

Fig. 4. In situ XRD patterns of the freshly reduced Au–Cu/SBA-15 catalyst with (a) time on stream at 80 °C and (b) increasing temperature under PROX atmosphere. The vertical lines indicate the 2θ position at 39.2°.

technique to characterize the Au–Cu/SBA-15 catalyst. EPR was reported to be very effective in identifying paramagnetic Cu^{2+} species, even in a trace amount [38]. Fig. 5 shows the EPR spectra of Au–Cu/SBA-15 after various thermal treatments. As shown by curve a, the as-calcined Au–Cu/SBA-15 catalyst presents four splitting features resulting from hyperfine coupling between the 3d unpaired electron and the copper ($I = 3/2$) nuclear spin [39]. The g and

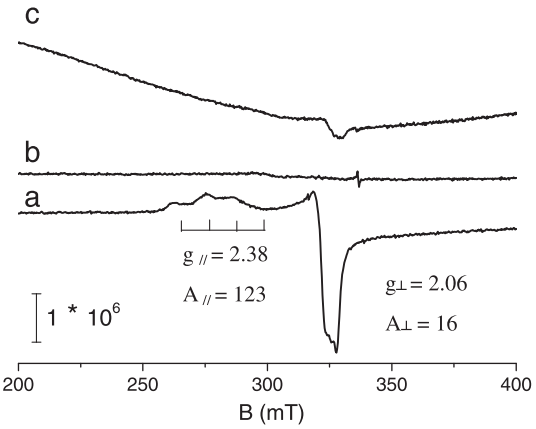

Fig. 5. In situ EPR spectra of Au–Cu/SBA-15 catalyst recorded at 150 K: (a) the as-calcined sample; (b) the freshly reduced sample; (c) the reduced sample was further treated at 400 °C for 0.5 h under CO oxidation atmosphere.

A parameters ($g_{//} = 2.38$, $A_{//} = 123$) are close to those of Cu^{2+} in octahedral coordination [40,41]. The perpendicular feature ($g\perp = 2.06$, $A_\perp = 16$) was not resolved. All these features are characteristic of Cu^{2+} cations. On the other hand, when the calcined catalyst was reduced at 550 °C in H_2, the EPR signals of Cu^{2+} cations completely disappeared (curve b). This result indicates that the Cu^{2+} has been reduced to EPR-silent low-valence Cu^+ or Cu^0, in consistence with the in situ XRD result that Au_3Cu_1 alloy phase was formed after the reduction at above 325 °C. When the reduced catalyst was further treated at 400 °C under the CO oxidation atmosphere with the presence of excess O_2, the EPR signals characteristic of Cu^{2+} appeared again, although with very weak intensity. The significantly reduced intensity of Cu^{2+} signal in comparison with the as-calcined sample might indicate that the majority of Cu^0 in the Au_3Cu_1 alloy phase was oxidized to EPR-silent Cu^+, while only a small part of Cu^0 was further oxidized to Cu^{2+} during the CO oxidation. This will be further confirmed by the following in situ XANES data.

3.4. In situ XANES

XANES spectroscopy is an ideal technique that can be used to determine the average oxidation state of metal components in the catalysts. The XANES spectra of the Au–Cu/SBA-15 catalyst, as-calcined and treated at different conditions, were measured respectively at the Au L_{III}-edge and Cu K-edge, and the results are shown in Fig. 6. For the spectra at the Au L_{III}-edge (Fig. 6A), they are very similar to that of the Au foil irrespective of the treatment conditions, indicating that Au in the Au–Cu bimetallic catalysts is very stable and remains at a metallic state (Au^0). On the other hand, the XANES spectra at the Cu K-edge are sensitive to the treatment conditions of the catalyst. As shown in Fig. 6B, the copper species in the as-calcined Au–Cu bimetallic catalyst are mainly composed of CuO, in agreement with the EPR result. After reduction treatment, in particular with increasing the reduction temperature up to 500 °C, the spectra show a combination feature of Cu foil and Cu_2O, indicating that Cu^{2+} has been reduced into low-valence Cu^0 and Cu^+. However, it is surprising that there is still a non-negligible amount of Cu^+ retained in the catalyst even after the reduction treatment at 500 °C. This part of difficultly reduced Cu^+ species is supposed to derive from the strong interaction between the silica surface and the Cu species. In our previous work about Au–Ag nanoparticles [28], we proposed that during calcination Ag was segregated on the surface and interacted with the silica support by oxygen linkage, just like a nano-glue to prevent the nanoparticles from aggregation/agglomeration [42]. Likewise, the same phenomena may occur on the Au–Cu nanoparticles. In other words, the Cu component in the as-calcined Au–Cu bimetallic sample prefers to residing on the particle surface as a copper oxide layer or patches while Au on the core. This is reasonable taking it into account that the gold particles had already formed prior to the deposition of copper. The part of copper oxide which is strongly interacted with the silica surface is difficult to reduce, and therefore cannot alloy with Au. Even at a very harsh reduction condition, this part of Cu species remains as Cu^+. This result is also consistent with the XRD conclusion that only one-third of the total Cu component is alloyed with Au. Meanwhile, we cannot exclude the possibility that there is a part of Cu existing as isolated monometallic Cu species. However, this part of Cu is inactive for CO oxidation.

Following the reduction treatment at 500 °C, the freshly reduced Au–Cu/SBA-15 catalyst was subsequently treated under CO oxidation atmosphere from RT to 300 °C, and the XANES spectra were measured in situ. As shown in Fig. 6B, after being treated by the mixture gas of CO and O_2, the spectra show a feature composed of Cu^{2+} and Cu^+, no matter what reaction temperature was used. This result is consistent with in situ XRD and EPR implications, suggesting that Cu^0 in the reduced Au–Cu alloy phase is

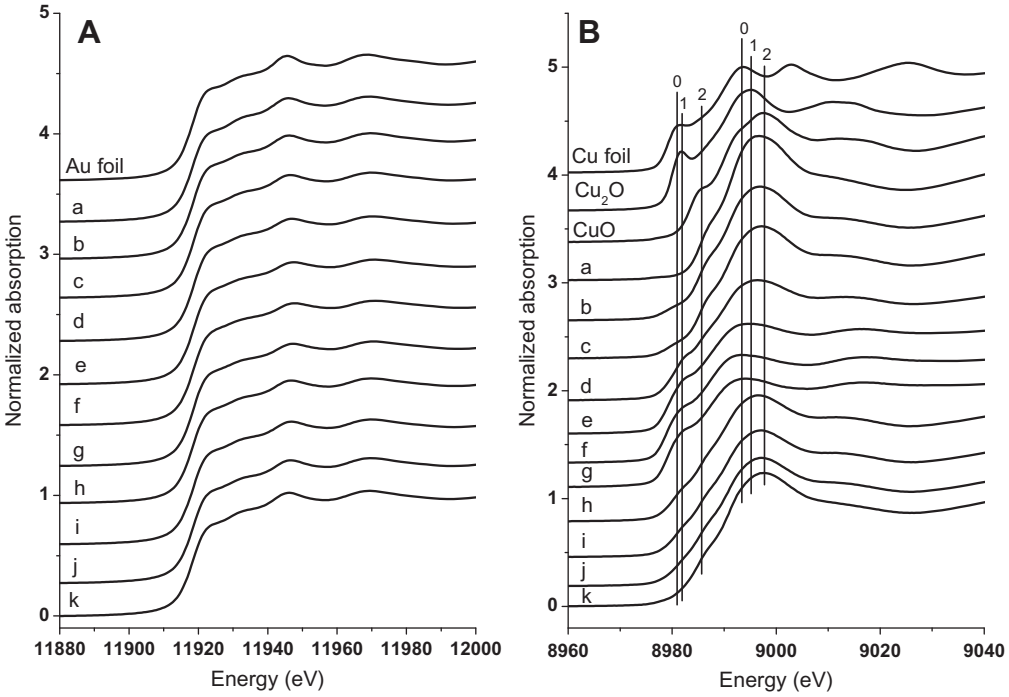

Fig. 6. Normalized XANES spectra at Au L_{III}-edge (A) and Cu K-edge (B) of Au–Cu/SBA-15 catalyst after treatment at various atmospheres and temperatures. Au foil and Cu foil as the references. The curves from a to k correspond to as-calcined (a), reduced at RT (b), 100 °C (c), 200 °C (d), 300 °C (e), 400 °C (f), and 500 °C (g); reacted in a typical CO oxidation atmosphere at RT for 18 h (h), 80 °C for 2 h (i), 160 °C for 2 h (j), and 300 °C for 2 h (k), respectively. The vertical lines in panel (B) show the positions of maximum absorption and shoulder feature for three Cu reference compounds, serving as a guide for easily tracing the spectral shift of the catalyst sample. The numbers 0, 1, and 2 represent Cu^0, Cu^+, and Cu^{2+}, respectively.

rather unstable under the CO oxidation atmosphere and is very easily oxidized into high-valence Cu^{2+} and Cu^+.

3.5. In situ IR spectra

3.5.1. In situ DRIFT at room temperature

In order to identify the surface species of the Au–Cu/SBA-15 which are responsible for the exceptionally high activity in CO oxidation, we used CO as a probe molecule to conduct in situ IR measurements. Fig. 7 presents the room-temperature DRIFT spectra of Au/SBA-15, Cu/SBA-15, and bimetallic Au–Cu/SBA-15 under CO alone or CO oxidation conditions. Under CO alone conditions, the adsorption of CO on Au/SBA-15 produced a band at 2116 cm^{-1}, while it was at 2120 cm^{-1} on Cu/SBA-15 and 2123 cm^{-1} on Au–Cu/SBA-15 (Fig. 7a). It was noted that at room temperature the adsorption of CO on these three samples was rather weak; purging with He for 30 min led to complete disappearance of the CO absorption bands.

Under CO oxidation conditions, the DRIFT spectra of Au/SBA-15 and Au–Cu/SBA-15 catalysts were very similar (Fig. 7b). The band due to CO adsorption on metallic Au^0 had a blue shift from 2116 cm^{-1} to 2122 cm^{-1}, which might be caused by the co-adsorption of CO and O_2 on the gold site [43]. In addition, a new band appeared at 2341 cm^{-1} which could be ascribed to CO_2 adsorbed on the surface of SBA-15. This result indicates that both catalysts are active for CO oxidation even at room temperature, and the Au–Cu/SBA-15 is more active as shown by the higher intensity of CO_2 absorption band. This result is in agreement with our previous report [30]. Different from either Au/SBA-15 or Au–Cu/SBA-15, the Cu/SBA-15 showed only one absorption band at 2120 cm^{-1}. The CO_2 absorption band was not observed since the Cu/SBA-15 was totally inactive for room-temperature CO oxidation [30]. To make correct assignments for the absorption bands at around 2120 cm^{-1} on the Cu/SBA-15 and Au–Cu/SBA-15 catalysts, the three catalysts were all purged with He following the CO oxidation. As shown in Fig. 7c, the CO absorption band on the Au/SBA-15 disappeared completely upon purging with He due to the weak adsorption of CO on Au^0 [44]. Quite different from the case of Au/SBA-15, the absorption band at 2120 cm^{-1} was still observable both on Cu/SBA-15 and on Au–Cu/SBA-15 after purging with He for 30 min, although the band position had a slight blue shift to 2123 cm^{-1}. It was reported that CO adsorption on either Cu^{2+} or metallic Cu^0 was very weak and easily removed by purging with inert gas at room temperature [45,43,46,47]. Therefore, the absorption band observed on the Cu/SBA-15 must be due to the CO adsorbed on Cu^+ [47–49]. For the Au–Cu/SBA-15, the band intensity was decreased significantly after purging with He, which means that the band is probably the superimposition of CO adsorbed on Cu^+, Cu^{2+}, and Au^0 sites, and the adsorption of CO on the latter two sites (Cu^{2+} and Au^0) is removed by He. The above DRIFT results strongly suggest that the metallic Cu^0 in the Au–Cu alloy nanoparticles was oxidized to Cu^+ and Cu^{2+} during the room-temperature CO oxidation reaction, which is in agreement with the in situ XANES and EPR results.

3.5.2. In situ FT-IR at a low temperature

The above room-temperature DRIFT spectra of CO adsorbed on Au–Cu/SBA-15 catalyst indicate that CO weakly adsorbs on both Au and Cu sites. In this case, it is still difficult to identify which sites are genuinely active for CO oxidation. To solve this problem, we recorded in situ FT-IR spectra of adsorbed CO at a low temperature (−110 °C). As shown in Fig. 8a, the adsorption of CO on Au/SBA-15 yielded a strong absorption band at 2100 cm^{-1}. After evacuation of gaseous CO (the peak blue shifts to 2102 cm^{-1}), O_2 was introduced into the cell. A strong absorption band characterizing the adsorbed CO_2 immediately appeared at 2341 cm^{-1}, and concomitantly there was a decrease in the intensity of CO absorption band. This result indicates that the CO adsorbed on metallic Au^0

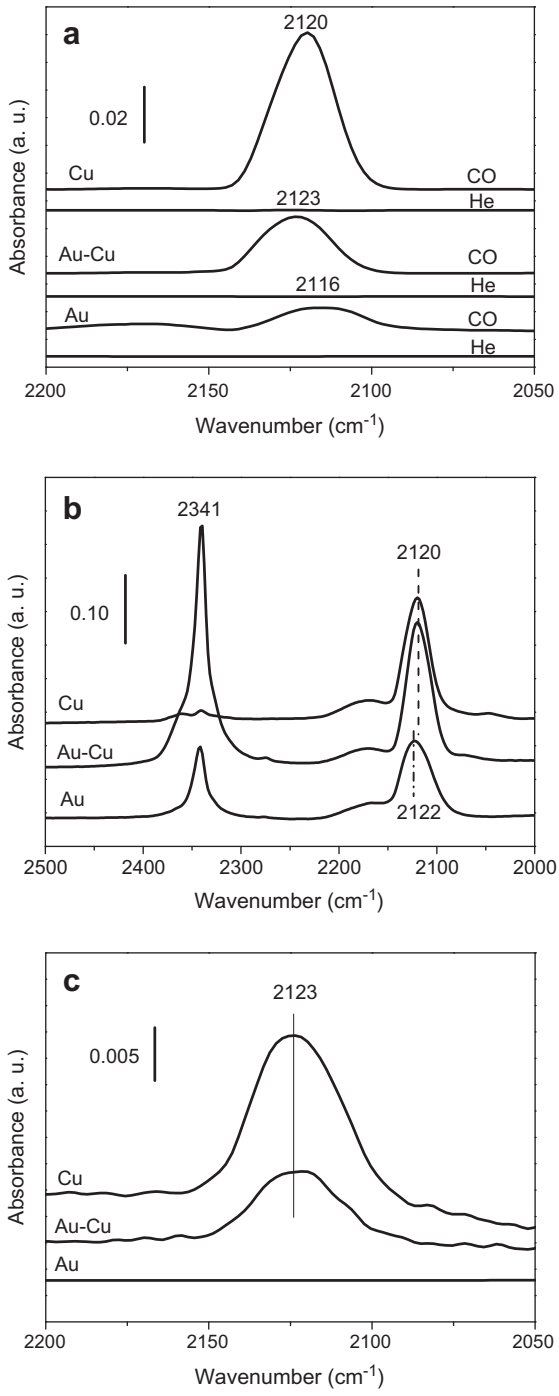

Fig. 7. In situ DRIFT spectra of CO adsorption on Au/SBA-15, Au–Cu/SBA-15, and Cu/SBA-15 at room temperature: (a) in CO atmosphere and followed by purging with pure He for 30 min; (b) in CO oxidation atmosphere; (c) purging with pure He for 30 min following the adsorption in CO oxidation atmosphere. Prior to the CO adsorption, the catalysts were pretreated in pure H_2 at 500 °C for 1 h.

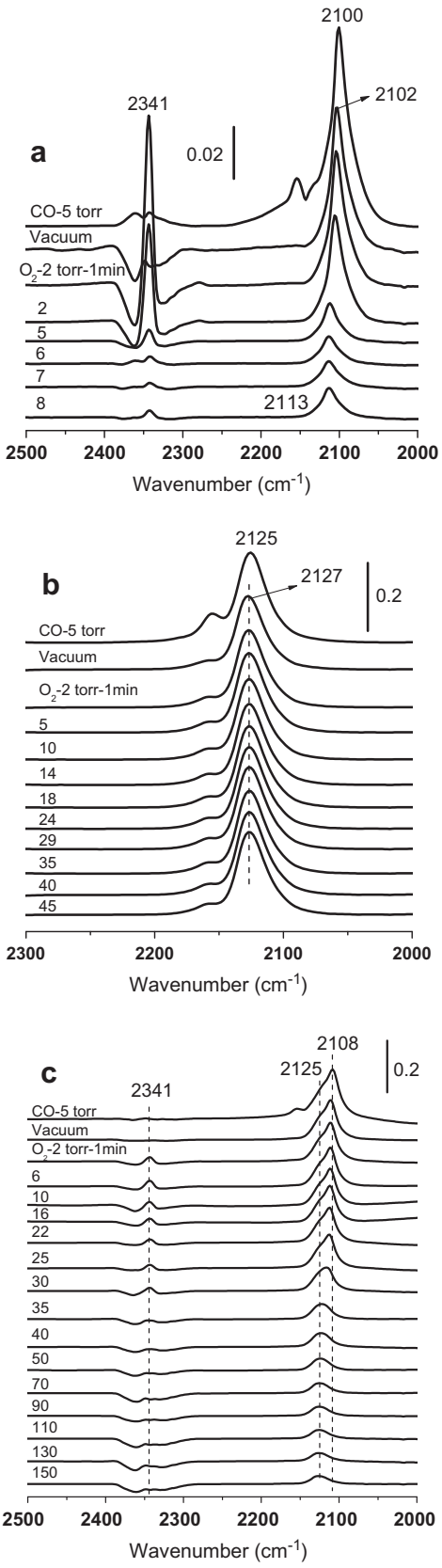

Fig. 8. In situ FT-IR spectra of CO adsorption on (a) Au/SBA-15, (b) Cu/SBA-15, and (c) Au–Cu/SBA-15 catalysts at −110 °C, followed by evacuation and introduction of O_2 gas for different periods. Prior to the CO adsorption, the catalysts were pretreated in pure H_2 at 500 °C for 1 h.

readily reacts with O_2 even at a temperature as low as −110 °C, in good agreement with the activity result we reported previously [30]. On the other hand, when O_2 was introduced following the CO adsorption on Cu/SBA-15, no substantial changes were observed (Fig. 8b), indicating that CO adsorbed on Cu sites is inactive toward reaction with O_2.

Different from the monometallic Au or Cu catalysts, when CO adsorbed on the bimetallic Au–Cu/SBA-15 catalyst, a strong absorption band at 2108 cm^{-1} together with a shoulder at 2125 cm^{-1} could be clearly observed. Based on the IR spectra of CO adsorbed on monometallic Au and Cu catalysts, the main absorption band at 2108 cm^{-1} can be ascribed to CO adsorbed on

Au^0 while the shoulder at 2125 cm^{-1} to CO adsorbed on metallic Cu^0. After introduction of O_2, the absorption band at 2108 cm^{-1} had a remarkable decrease with time and disappeared completely after 70 min, while the absorption band at 2125 cm^{-1} remained unchanged (Fig. 8c). At the same time, an intense absorption band of adsorbed CO_2 appeared upon introduction of O_2. This result provides strong evidence that Au^0, either in the monometallic Au/SBA-15 or in the bimetallic Au–Cu/SBA-15, indeed functions as the active site for CO oxidation.

4. Discussion

4.1. Structural changes of the Au–Cu bimetallic nanoparticles

Au–Cu bimetallic nanoparticles have been reported to outperform their monometallic counterparts in a variety of industrially important oxidation reactions [50]. For example, Llorca and coworkers investigated Au–Cu/TiO_2 catalysts for propene epoxidation with N_2O, and found that Au_1Cu_3/TiO_2 gave the best performance [51]. Pina et al. explored Au–Cu/SiO_2 catalyst for the selective oxidation of benzyl alcohol, and observed synergistic effect at Au/Cu weight ratio of 4/1 [52]. However, the structural changes during these oxidation reactions have not been considered yet. In this work, through a combination of in situ techniques, we tried to give a clear image about the structural changes of the catalyst in different pretreatment and reaction atmospheres. Since the gold particles had already formed before the deposition of copper during our two-step synthesis procedure, we proposed that a core–shell like structure was probably constructed at the initial stage. After the calcination treatment, the copper on the surface would be oxidized. Thus, the as-calcined bimetallic nanoparticles are composed of a gold core which is surrounded by a CuO layer or patches of CuO. The structure at this stage is illustrated in Fig. 9a. Both EPR and XANES of the as-calcined sample provided consistent evidence of Cu^{2+}, and the XRD identified the pure gold phase instead of gold–copper alloy phase. Upon reduction treatment with a temperature-increased mode, the CuO surface layer/patches were reduced into low-valence Cu^+ and Cu^0, and the Cu^0 diffused into gold core and finally formed an Au_3Cu_1 intermetallic phase, while the Cu^+ interacts strongly with the support and plays an important role in limiting the movement and agglomeration of the particles, as illustrated in Fig. 9b. When the Au_3Cu_1 intermetallic phase was exposed to a reaction atmosphere composed of CO and O_2, the Cu^0 component in the intermetallic phase was oxidized into Cu^+ and Cu^{2+} and again segregated on the surface to form the gold core/CuO_x patches, as illustrated in Fig. 9c. The DRIFT, EPR, XRD, and XANES characterizations all confirm the structural changes depicted in Fig. 9.

4.2. Active sites in CO oxidation

There are a large number of works discussing the active sites of supported gold catalysts in CO oxidation, the proposed reaction sites include cationic gold species [53,54], bilayer gold clusters composed of less than 10 atoms [55,56], and the junction perimeter between gold and the metal oxide support [57]. In the case of Au–Cu bimetallic catalysts, we did not detect any cationic gold species in either pretreated catalyst or working catalyst; only Au^0 was identified by both IR and XANES examinations. On the other hand, the FT-IR spectra provide strong evidence that the CO adsorbed on Au^0 reacted facilely with O_2 to produce CO_2 even at the temperature as low as −110 °C, while the CO adsorbed on Cu^+/Cu^{2+} just as a spectator. Therefore, we can conclude that in both monometallic Au and bimetallic Au–Cu catalysts, the active sites for CO oxidation are Au^0 sites. This conclusion is also supported by the inactivity of Cu/SBA-15 for CO oxidation [30,31]. However, why did the Au–Cu bimetallic catalyst show a much higher activity than the monometallic Au catalyst? In the previous work [30,31], we have shown that the particle size of the Au–Cu bimetallic catalyst is significantly smaller than the monometallic Au catalyst due to the sintering-resistant contribution of Cu species, which, we believe, is one reason for the enhanced activity of the Au–Cu bimetallic catalyst. However, a more important reason should be the role of Cu species in activating oxygen. It is known that the activation of O_2 is a key step in gold-catalyzed low-temperature CO oxidation [58,59]. For gold nanoparticles supported on a reducible oxide (e.g., TiO_2, FeO_x, CeO_2, etc.), the active oxygen is provided by metal oxide support and the reaction is proposed to occur at the perimeter between the gold particles and the oxide support [57]. In the bimetallic Au–Cu catalyst, we used SBA-15 as the support which cannot provide active oxygen. However, we found that Cu^0 in the bimetallic Au–Cu catalyst was easily oxidized into Cu^+ and Cu^{2+} under CO oxidation conditions, which strongly suggests that oxygen can be activated at the Cu sites. At the steady CO oxidation condition, the Au–Cu bimetallic structure is actually an inverse Au/CuO_x structure where patches of CuO_x are supported on the surface of gold particles (Fig. 9c). Since the gold particle size is only 2–3 nm [30], one can imagine that the patches of CuO_x should be very small even in a subnanometer range. In this case, the perimeter between the gold and the CuO_x patches is very large, which will boost the reaction occurred at the perimeter. Therefore, we can conclude that the Cu component in the Au–Cu bimetallic catalyst plays dual roles: one is to anchor the gold particles on the silica support and the other is to provide reactive oxygen for CO oxidation. Both functions are strongly dependent on the segregation of Cu component to form CuO_x species on the surface of gold particles.

The earlier discussions have also some implications on the reaction nature of the recently reported nanoporous gold [60]. In nanoporous gold, it was found that the catalytic activity was strongly associated with the residual amount of silver, and silver was significantly enriched on the surface. Actually, Haruta [61] proposed that the active structure of the nanoporous gold is composed of Ag_2O patches dispersed on the gold surface, very similar to our Au–Cu bimetallic structure depicted in Fig. 9c.

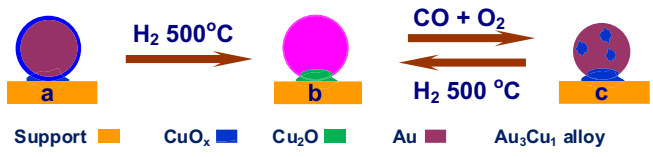

Fig. 9. Schematic illustration of the structural changes of the Au–Cu/SBA-15 under H_2 reduction and CO oxidation conditions.

5. Conclusions

In summary, we have provided a clear image about the structural changes of SBA-15 supported Au–Cu bimetallic nanoparticles under different pretreatment and CO oxidation reaction conditions, by using in situ XRD, EPR, FT-IR, and XANES techniques. The as-calcined catalyst is composed of gold core decorated by a layer or patches of CuO. After being pretreated (activated) with H_2 at a high temperature, a part of the CuO was reduced into metallic Cu^0 and diffused into gold core to form Au_3Cu_1 alloy phase, while the other part of CuO which was directly interacted with the support was only reduced to Cu^+ acting as the nano-glue between Au_3Cu_1 particles and the support. During CO oxidation, the Cu^0 component was enriched on the surface and form CuO_x tiny patches on the gold surface, thus maximizing the perimeter between gold and CuO_x. CO adsorbed on gold reacts with the active oxygen provided

by the neighboring CuO_x, in this way the catalytic activity was enhanced greatly in comparison with monometallic gold. The structural changes demonstrated in this work is not unique for the Au–Cu bimetallic catalyst, but can also be extended to other gold-containing bimetallic catalysts such as Au–Ag and Au–Pd systems. More importantly, the combination of in situ techniques provides insightful understanding of the catalysis mechanism of gold-alloy catalyst and directs us to design more active and selective bimetallic catalysts.

Acknowledgment

Supports from the National Natural Science Foundation of China (NNSFC 20773124 and 20803079) are gratefully acknowledged.

References

[1] M. Chen, D. Kumar, C.W. Yi, D.W. Goodman, Science 310 (2005) 291.
[2] D.I. Enache, J.K. Edwards, P. Landon, B. Solsona-Espriu, A.F. Carley, A.A. Herzing, M. Watanabe, C.J. Kiely, D.W. Knight, G.J. Hutchings, Science 311 (2006) 362.
[3] W.C. Ketchie, M. Murayama, R.J. Davis, J. Catal. 250 (2007) 264.
[4] M. Conte, A.F. Carley, G. Attard, A.A. Herzing, C.J. Kiely, G.J. Hutchings, J. Catal. 257 (2008) 190.
[5] Y.L. Hsin, K.C. Hwang, C.T. Yeh, J. Am. Chem. Soc. 129 (2007) 9999.
[6] L.L. Mickelson, C. Friesen, J. Am. Chem. Soc. 131 (2009) 14879.
[7] M.L. Lin, M.Y. Lo, C.Y. Mou, J. Phys. Chem. C 113 (2009) 16158.
[8] R.N. Lamb, B. Ngamsom, D.L. Trimm, B. Gong, P.L. Silveston, P. Praserthdam, Appl. Catal. A: Gen. 268 (2004) 43–54.
[9] P.A. Sheth, M. Neurock, C.M. Smith, J. Phys. Chem. B 109 (2005) 12449.
[10] S.A. Nikolaev, L.N. Zanaveskin, V.V. Smirnov, V.A. Averyanov, K.L. Zanaveskin, Russ. Chem. Rev. 78 (2009) 231.
[11] D. Zhao, B.Q. Xu, Angew. Chem. Int. Ed. 45 (2006) 4955.
[12] J. Zhang, K. Sasaki, E. Sutter, R.R. Adzic, Science 315 (2007) 220.
[13] J.G. Chen, C.A. Menning, M.B. Zellner, Surf. Sci. Rep. 63 (2008) 201.
[14] A. Alayoglu, A.U. Nilekar, M. Mavrikakis, B. Eichhorn, Nat. Mater. 7 (2008) 333.
[15] F. Tao, M.E. Grass, Y. Zhang, D.R. Butcher, J.R. Renzas, Z. Liu, J.Y. Chung, B.S. Mun, M. Salmeron, G.A. Somorjai, Science 322 (2008) 932.
[16] R. Ferrando, J. Jellinek, R.L. Johnston, Chem. Rev. 108 (2008) 845.
[17] M. Haruta, T. Kobayashi, H. Sano, N. Yamada, Chem. Lett. (1987) 405.
[18] G.C. Bond, D.T. Thompson, Catal. Rev. Sci. Eng. 41 (1999) 319.
[19] A. Stephen, K. Hashmi, G.J. Hutchings, Angew. Chem. Int. Ed. 45 (2006) 7896.
[20] J. Huang, T. Akita, J. Faye, T. Fujitani, T. Takei, M. Haruta, Angew. Chem. Int. Ed. 48 (2009) 7862.
[21] P. Landon, P.J. Collier, A.J. Papworth, C.J. Kiely, G.J. Hutchings, Chem. Commun. (2002) 2058.
[22] H. Miyamura, R. Matsubara, Y. Miyazaki, S. Kobayashi, Angew. Chem. Int. Ed. 46 (2007) 4151.
[23] S. Zhou, H. Yin, V. Schwartz, Z. Wu, D. Mullins, B. Eichhorn, S.H. Overbury, S. Dai, Chem. Phys. Chem. 9 (2008) 2475.
[24] J.H. Liu, A.Q. Wang, Y.S. Chi, H.P. Lin, C.Y. Mou, J. Phys. Chem. B 109 (2004) 40.
[25] A.Q. Wang, J.H. Liu, S.D. Lin, T.S. Lin, C.Y. Mou, J. Catal. 233 (2005) 186.
[26] A.Q. Wang, Y.P. Hsieh, Y.F. Chen, C.Y. Mou, J. Catal. 237 (2006) 197.
[27] A.Q. Wang, C.M. Chang, C.Y. Mou, J. Phys. Chem. B 109 (2005) 18860.
[28] X. Liu, A. Wang, X. Yang, T. Zhang, C.Y. Mou, D.S. Su, J. Li, Chem. Mater. 21 (2009) 410.
[29] C.W. Yen, M.L. Lin, A.Q. Wang, C.Y. Mou, J. Phys. Chem. C 113 (2009) 17831.
[30] X. Liu, A. Wang, X. Wang, C.Y. Mou, T. Zhang, Chem. Commun. (2008) 3187.
[31] X. Liu, A. Wang, T. Zhang, D.S. Su, C.Y. Mou, Catal. Today (2010), doi:10.1016/j.cattod.2010.05.019.
[32] Y. Nishihata, J. Mizuki, T. Akao, H. Tanaka, M. Uenishi, M. Kimura, T. Okamoto, N. Hamada, Nature 418 (2002) 164.
[33] D. Zhao, Q. Huo, J. Feng, B.F. Chmelka, G.D. Stucky, J. Am. Chem. Soc. 120 (1998) 6024.
[34] B. Ravel, M. Newville, J. Synch. Rad. 12 (2005) 537.
[35] C.W. Chiang, A. Wang, B.Z. Wan, C.Y. Mou, J. Phys. Chem. B 109 (2005) 18042.
[36] S. Pal, G. De, J. Mater. Chem. 17 (2007) 493.
[37] G. De, C.N.R. Rao, J. Phys. Chem. B 107 (2003) 13597.
[38] A. Gervasini, M. Manzoli, G. Martra, A. Ponti, N. Ravasio, L. Sordelli, F. Zaccheria, J. Phys. Chem. B 110 (2006) 7851.
[39] S.C. Larsen, A. Aylor, A.T. Bell, J.A. Reimer, J. Phys. Chem. 98 (1994) 11533.
[40] P. Decyk, Catal. Today 114 (2006) 142.
[41] Y. Li, D. An, Q. Zhang, Y. Wang, J. Phys. Chem. C 112 (2008) 13700.
[42] M.M. Schubert, M.J. Kahlich, G. Feldmeyer, M. Hüttner, S. Hackenberg, H.A. Gasteiger, R.J. Behm, Phys. Chem. Chem. Phys. 3 (2001) 1123.
[43] Z. Wu, S. Zhou, H. Zhu, S. Dai, S.H. Overbury, Chem. Commun. (2008) 3308.
[44] M. Mihaylov, H. Knözinger, K. Hadjiivanov, B.C. Gates, Chem. Ing. Tech. 79 (2007) 795.
[45] D. Mott, J. Luo, A. Smith, Nanoscale Res. Lett. 2 (2007) 12.
[46] Z. Wu, S. Zhou, H. Zhu, S. Dai, S.H. Overbury, J. Phys. Chem. C 113 (2009) 3726.
[47] K. Hadjiivanov, T. Tsoncheva, M. Dimitrov, C. Minchev, H. Knözinger, Appl. Catal. A: Gen. 241 (2003) 331.
[48] A. Dandekar, M.A. Vannice, J. Catal. 178 (1998) 621.
[49] C.S. Chen, J.H. Lin, T.W. Lai, Chem. Commun. (2008) 4983.
[50] C.L. Bracey, P.R. Ellis, G.J. Hutchings, Chem. Soc. Rev. 38 (2009) 2231.
[51] J. Llorca, M. Domínguez, C. Ledesma, R.J. Chimentão, F. Medina, J. Sueiras, I. Angurell, M. Seco, O. Rossell, J. Catal. 258 (2008) 187.
[52] C.D. Pina, E. Falletta, M. Rossi, J. Catal. 260 (2008) 384.
[53] J.C. Fierro-Gonzalez, J. Guzman, B.C. Gates, Top. Catal. 44 (2007) 103.
[54] M.C. Kung, R.J. Davis, H.H. Kung, J. Phys. Chem. C 111 (2007) 11767.
[55] M.S. Chen, D.W. Goodman, Science 306 (2004) 252.
[56] A.A. Herzing, C.J. Kiely, A.F. Carley, P. Landon, G.J. Hutchings, Science 321 (2008) 1331.
[57] M. Haruta, Chem. Record 3 (2003) 75.
[58] M.M. Schubert, S. Hackenberg, A.C. Veen, M. Muhler, V. Plzak, R.J. Behm, J. Catal. 197 (2001) 113.
[59] M. Daté, M. Okumura, S. Tsubota, M. Haruta, Angew. Chem. Int. Ed. 43 (2004) 2129.
[60] A. Wittstock, J. Biener, M. Bäumer, Phys. Chem. Chem. Phys. 12 (2010) 12919.
[61] M. Haruta, ChemPhysChem 8 (2007) 1911.